Flexural performance of composite beam with high-strength steel girder and ECC slab: A comprehensive parametric study

Anh-Duc Mai, Chi-King Lee, Cong-Luyen Nguyen

To cite this article

Disclaimer

Flexural performance of composite beam with high-strength steel girder and ECC slab: A comprehensive parametric study

Anh-Duc Mai [1,a], Chi-King Lee [2,b], Cong-Luyen Nguyen [*,3,c]

[1]Construction Management Division, The University of Danang – University of Science and Technology, Danang 550000, Vietnam
[2]School of Engineering and Technology, The University of New South Wales, Canberra, ACT 2600, Australia
[3]Construction Informatics Division, The University of Danang – University of Science and Technology, Danang 550000, Vietnam

Article Info	Abstract
	The combination of high-strength steel (HSS) girder and engineered cementitious composites (ECC) slab in composite beam exhibits excellent structural performance with enhanced strength and superior ductility. However, the effects of different parameters on the structural performance of this type of composite beam have yet to be thoroughly investigated. This study presents a numerical parametric study on the flexural performance of composite beams made of HSS girder and ECC slab. A validated numerical model developed by the authors using finite element ABAQUS software was adopted for the parametric investigation. The material nonlinearities and real contact between components were incorporated into the model. The effects of crucial parameters on the flexural performance of this composite beam type were examined based on the modelling results of total 136 HSS-ECC composite beam models. These key parameters consist of the mechanical properties of HSS and ECC materials, cross-section parameters, construction details, shear connection degree, and slab type. The bending performance of the composite beams was represented by initial bending stiffness, rotation, and normalized bending moment capacity. The results of parametric investigations revealed that the initial bending stiffness, rotation capacity, and normalized bending moment capacity of the modelled composite beams were sensitive to the mechanical properties of constitutive materials, cross-section dimensions, and construction details. It was also found that the slab type had a marginal effect on the flexural performance of HSS-ECC beams, while shear stud spacing significantly affected all the investigated indicators.

1. Introduction

Steel grades with a yield strength greater than 550 MPa are categorized as high-strength steel (HSS), which has become increasingly popular in structural engineering applications thanks to its advantage of high strength/weight ratio. Smaller in dimension, lighter in weight and greater in strength of HSS could reduce the construction cost owing to a significant reduction in welding, fabrication, and erection. As a result, HSS can be applied in various types of structures, including bare steel and composite columns [1-10], connections [11-15], encased beams [16-19]. It is evident from these studies that HSS has been utilized with its favorable strength, which led to the enhancement of structural performance. For a composite beam made of HSS girder connected with normal concrete slab through means of shear studs, when it is subjected to a sagging moment, a

HSS I-section is used at the bottom and plays a role in carrying tension, while in contrast, the concrete slab is placed on top of the steel I-section and resists compressive internal load. Thus, each material is employed in an efficient way as its favorable attributes are being fully utilized. If HSS is used to replace normal strength steel (NSS) I-section, the composite beam can theoretically take advantage of the superior strength of HSS. However, experimental [20,21], numerical [22,23], and analytical [24,25] studies on HSS-concrete composite beams reported that sudden crushing of concrete slab in bending region could occur, and the HSS-concrete composite beam could not reach its plastic strength capacity due to strain incompatibility between HSS and concrete. To be more specific, higher strain capacity of HSS at the bottom (0.35% for HSS grade 690 MPa) versus lower strain of concrete (0.23% - 0.3%) could result in a premature crushing of concrete, and thus, the superior strength of HSS could not be employed [20-25]. Furthermore, longitudinal shear failure may occur in a concrete composite beam utilizing an HSS I-section due to an imbalance longitudinal shear load between the HSS I-section and the normal concrete slab if the slab is transversely reinforced inadequately [26,27]. As a result, the bending capacity of the beam constructed with HSS girder and concrete slab is even lower than the case having a failure mode of concrete crushing in the bending area as longitudinal shear failure occurred at the very early stage of the loading process [27].

To address aforementioned drawback of composite beam made of HSS girder and concrete slab, Nguyen and Lee [28] recently proposed a novel composite beam based on two constitutive materials of HSS and ECC, in which ECC slab was employed to replace concrete slab on top connected with HSS I-section at the bottom by shear studs. Indeed, ECC possesses high compressive strain capacity (over 0.5%, which is higher than any HSS grades available to date), allowing it to resist the compressive load in the slab until HSS reaches its full strength. Besides, high shear resistance and better bond strength of ECC help prevent longitudinal shear failure [29-30]. On top of that, employing HSS-ECC composite beams could substantially reduce embodied carbon content and carbon footprint since bi-products of steel and ferrosilicon alloy producing processes (i.e., fly ash, silica fume) are utilized to partially replace cement in the ECC mix which normally includes cement, fly ash, silica fume, sand, fiber, water, superplasticizer [31-34]. To examine the bending behavior of composite beam made of HSS girder and ECC slab (hereafter referred as HSS-ECC beam for brevity), Nguyen and Lee [28] conducted a four-point bending test of four beams, including three HSS-ECC beams manufactured with different slab thicknesses and compressive strengths of ECC, and one NSC-HSS beam used as a control beam. The results found that HSS-ECC beams demonstrated a great enhancement in flexural strength and ductility compared to HSS-concrete counterparts, which showed a failure mode of brutal crushing of concrete in the bending region. In addition, to complement the experimental result, a numerical finite element (FE) model as well as an analytical model have been constructed and validated against experimental findings [35]. It has been revealed that although the bending behavior of HSS-ECC beams has received attention from researchers recently [28,35], available studies on the bending behavior of HSS-ECC beams are very limited. In order to promote this type of composite beam to be widely applied in practical (e.g., structures under extreme conditions such as long span structures or structures subjected to high loading), an insight into the influence of different crucial parameters on the bending behavior of HSS-ECC beam is required. Thus, a parametric investigation on the flexural performance of HSS-ECC beams is essentially needed.

In this study, the finite element (FE) model using ABAQUS developed and validated by Nguyen and Lee [28], which has been proven as a reliable and accurate model for simulating the bending behavior of HSS-ECC beams, was used to conduct the parametric investigation. A total of 136 HSS-ECC beam models were generated and investigated to elucidate the effect of different parameters (i.e., mechanical properties of HSS and ECC materials, cross-section parameters, construction details, shear connection degree, and slab type) on their flexural performance represented by initial bending stiffness, rotation, and flexural capacities. The influences of these parameters were then discussed based on the numerical results.

2. The Validated Finite Element Model Adopted

This parametric investigation employs a verified nonlinear finite element (FE) model reported in the author's previous study [28]. The mentioned FE model was built using ABAQUS software with details of modelling and validation processes. Thus, the following sections will only summarize the key features of the model.

2.1. Element Types

The full model of HSS-ECC beam is used to realistically reflect the actual condition of the beams. Figure 1(a) indicates typical cross-section dimensions of the HSS-ECC beam. Solid elements C3D8R is employed to simulate the HSS, ECC, shear stud, and strengthened bolts [Figure 1(b)] as it is expected to minimize convergence issue and use less computational cost in comparison to other types of elements, such as tetrahedra C3D4. Four-node shell element S4R is utilized for simulating profiled steel sheeting (PSS) while truss element T3D2 is deployed for the steel meshes.
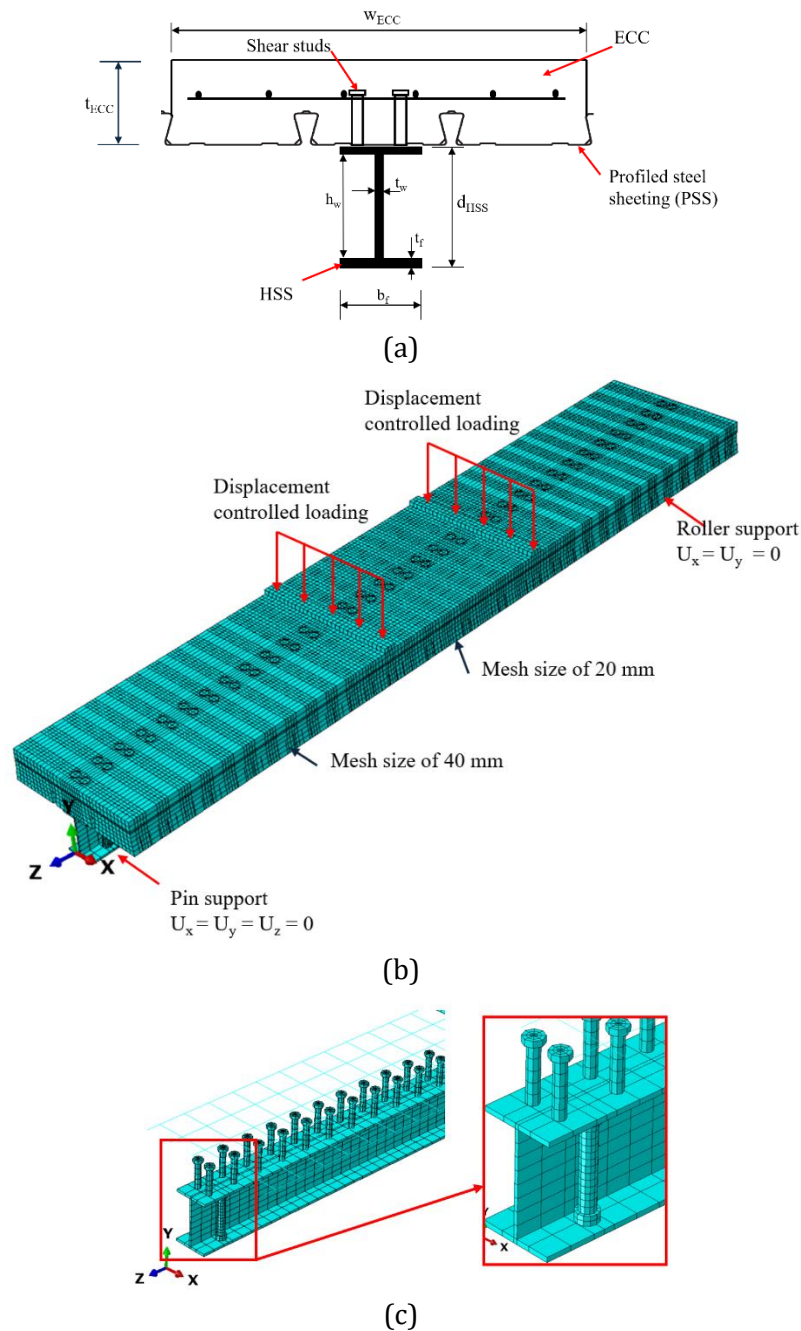

(a)

(b)

(c)

Fig. 1. HSS-ECC beam and FE model: (a) Typical cross-section configuration; (b) Typical FE model, (c) Partition method for components

2.2. Mesh Sizes

The mesh sizes used for HSS I-section is 40 mm and this guarantees that it is divided into more than 8 elements along the web of the HSS I-section [Figure 1(c)]. For its flange, it should be discretised in such a way that at least one common node between flange and centre point of shear stud's base [Figure 1(c)]. The nominal element size of shear stud, PSS and bar mesh, strengthened bolts are respectively 10 mm, 40 mm, 100 mm and 5 mm. After a mesh sensitivity analysis [28], mesh sizes for ECC slab in two shear spans and in the bending region are respectively 40 mm and 20 mm, as seen in Figure 1(b).

2.3. Interaction Properties Between Components

The interactions between HSS I-beam and PSS, between ECC slab and shear studs, between ECC slab and PSS were simulated using surface-to-surface contact available in ABAQUS [36]. The interaction between the HSS section top flange and the shear studs bottom was simulated using Tie constraint as shear stud is welded to HSS's top flange through resistance welding. This interaction type is also used for the contact between loading plates and the ECC slab. Embedded region available in ABAQUS [30] is utilised for the connection properties between the reinforcement mesh and ECC slab.

2.4. Constitutive models

Tensile and compression stress-strain models of ECC, which were suggested by Meng et al. [37], are adopted in the numerical modelling [Figure 2(a)-(c)]. For HSS section, its constitutive model indicated in Figure 2(d) is represented by a bilinear curve. The PSS is modelled using elastic-perfectly plastic curve that has been widely adopted in other studies [38], and shown in Figure 2(e). Regarding shear stud, as it is experimentally proven to have an excellent ductility, a constitutive model [Figure 2(f)] developed by Hassan et al. [39] is used. Mechanical properties of key materials employed in the constitutive models corresponding to the tests reported in [28] are listed Tables 1–2. These values were employed in the model validation and are the baseline values for the parametric investigation.

(a)

(b)

(c)

(d)

(e)

(f)

(g)
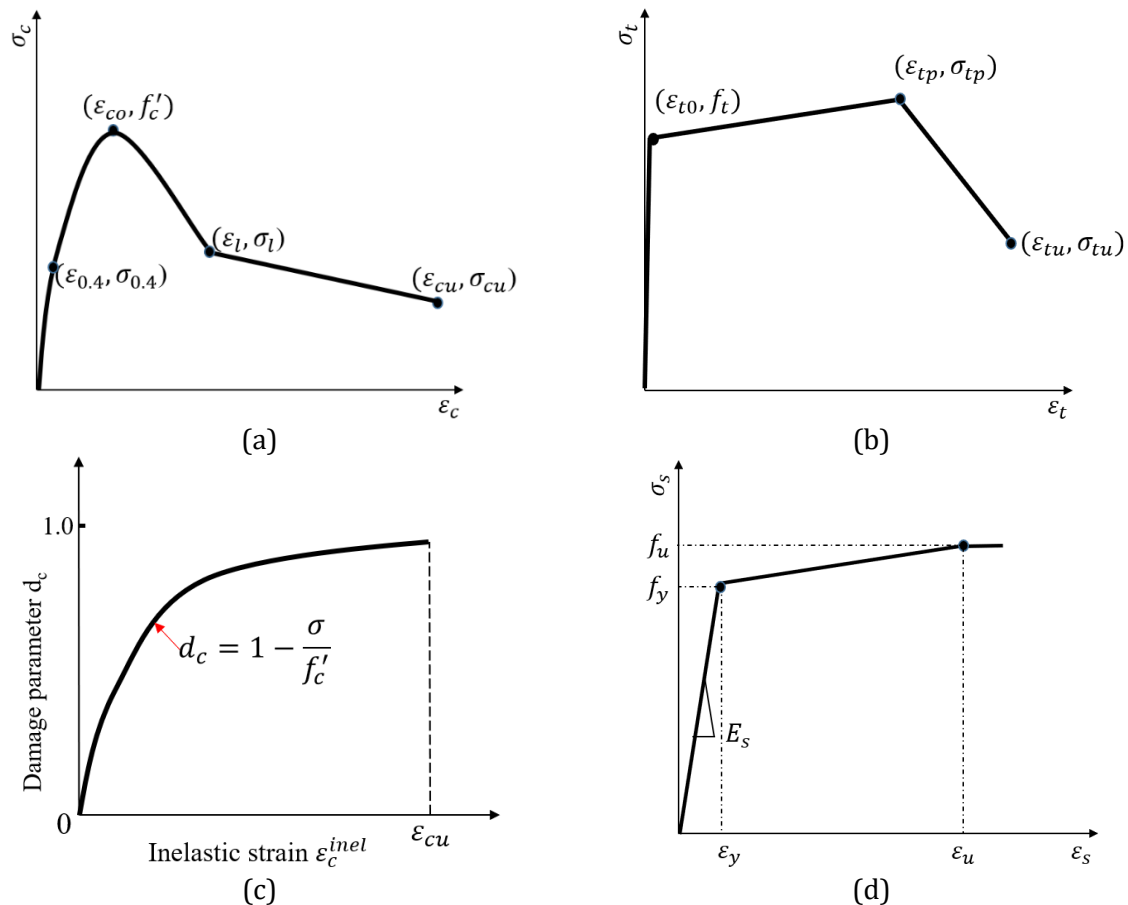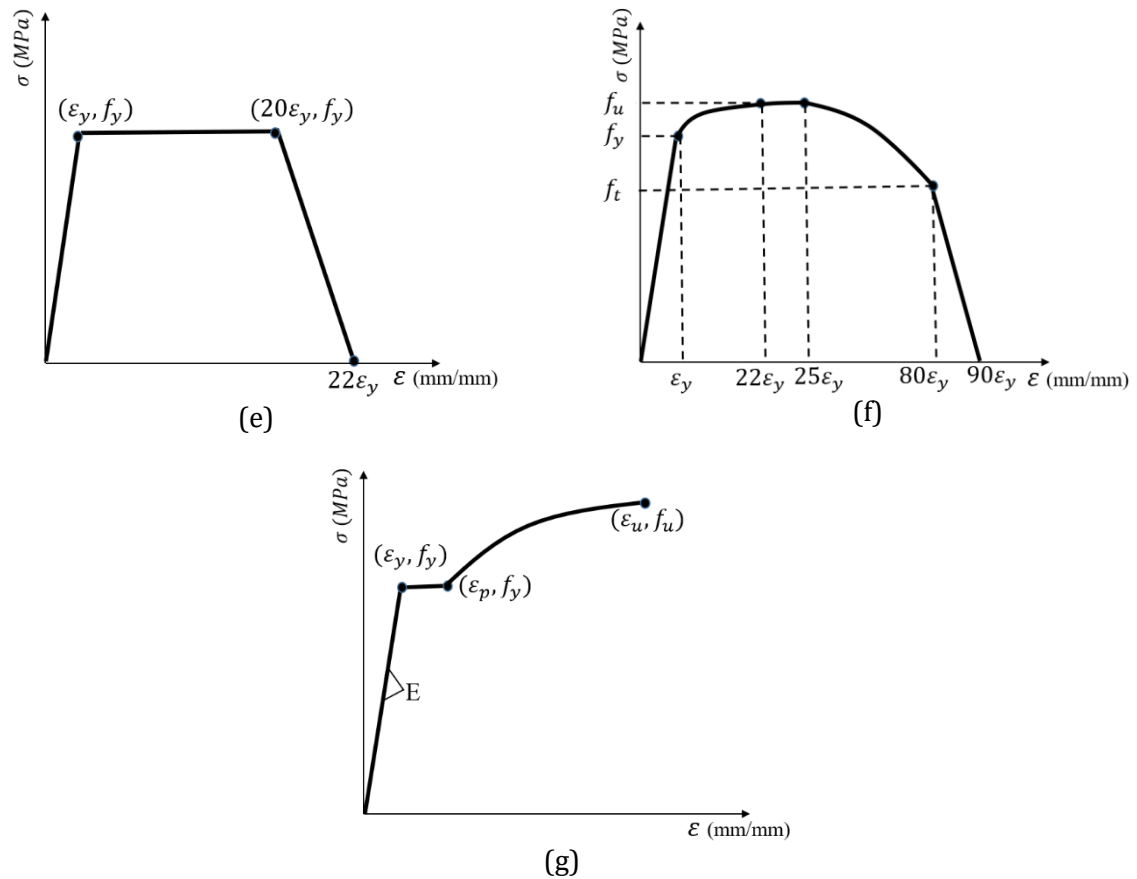
Fig. 2. Stress–strain models of materials for parametric investigation. (a) ECC stress-strain model under compression; (b) ECC stress-strain model under tensile; (c) ECC damage model under compression; (d) HSS; (e) PSS; (f) Headed shear stud; (g) Steel reinforcement

Table 1. Properties of materials for FE model

Material	E (GPa)	f_y (MPa)	f_u (MPa)	f_t (MPa)	ε_y(%)	ε_p(%)	ε_u(%)
Shear stud	200	344	410	331	0.17	-	-
PSS	248	691	-	-	0.28	-	-
Steel mesh	200	543	632	-	0.27	2.4	20.8
HSS Grade 690	200	690	770	-	0.35	-	8.0
HSS Grade 960	200	960	980	-	0.48	-	5.5

Table 2. ECC properties for FE model

Material	E_c (GPa)	$\sigma_{0.4}$ (MPa)	σ_{co} (MPa)	σ_l (MPa)	σ_{cu} (MPa)	$\varepsilon_{0.4}$ (%)	ε_{co} (%)	ε_l (%)	ε_{cu} (%)
CF40	15.5	16.0	40.0	20.0	10.0	0.10	0.50	0.85	1.20
CF70	20.5	28.0	70.0	30.0	13.5	0.14	0.53	0.95	1.40

Table 2. ECC properties for FE model (continued)

Material	σ_{to} (MPa)	σ_{tp} (MPa)	σ_{tu} (MPa)	ε_{to} (%)	ε_{tp} (%)	ε_{tu} (%)
CF40	2.43	3.2	1.7	0.016	1.2	2.2
CF70	4.40	5.3	3.0	0.021	1.0	1.7

2.5. Loading and Boundary Conditions

As simple supported beams with two loading points were employed in the experimental program [28], pin and roller supports are modelled in the simulation by restraining either two or three translational directions. Load is applied to those nodes located on the surface of the two loading points by applying downward displacement with the rate similar the rate that were used in the test [Figure 1(b)]. The self-weight is also applied in the simulation by inclusion of self-weight in the first step and propagated to the remaining steps of the simulation process.

By comparing with the test results, it was shown that the developed FE model has successfully captured the test results. The failure mode of HSS-ECC beams was that the large proportion of HSS at middle region was yielded before ECC top surface crushing (Figure 3), which is well-agreed with the test results reported in [28]. In addition, load (P)-mid-span deformation (δ) curves (hereafter referred as $P - \delta$ curves for brevity) obtained from all of the tested beams were confirmed by the verified FE model, not only in terms of bending capacity but also the bending stiffness. Thus, in this study, this verified nonlinear FE model is employed for the parametric analysis.

3. Parametric Investigation Design

The parametric analysis explored a broad spectrum of crucial parameters that influence the bending performance of HSS-ECC beams. A total of nine parameters were classified into three groups consisting of mechanical properties of materials [i.e., (1) ECC compressive strength, f'_{ECC} and (2) HSS tensile strength, $f_{y,HSS}$], cross-sectional dimension [i.e., (3) HSS section depth, d_{HSS}; (4-5) ECC slab thickness and width, t_{ECC}, w_{ECC}, respectively] (see Figure 1(a)) and construction details [e.g., (6) ratio of HSS section flange width and thickness, b_f/t_f; (7) ratio of HSS section web height and thickness, h_w/t_w; (8) shear stud spacing, s_{stud} and (9) ECC slab type].

For the mechanical properties of materials, two values of f'_{ECC} (i.e., 40 MPa and 70 MPa) and two values of $f_{y,HSS}$ (i.e., 690 MPa and 960 MPa) were considered. For cross-section dimensions, the w_{ECC} was varied from 600 to 1400 mm with an interval of 400 mm, the t_{ECC} was changed from 140 to 200 mm with an interval of 30 mm and the d_{HSS} was varied from 180 to 280 mm with an interval of 50 mm. For the construction details, three values of b_f/t_f of 10, 12 and 15; three values of the h_w/t_w of 16, 20 and 27, three values of the s_{stud} of 75, 100 and 200 mm and two types of ECC slab including profiled steel sheeting (PSS) and solid slab were utilized.

If all possible combinations of the nine parameters listed above were modelled, it would require creating a total of 5,832 models (calculated as 2×2×3×3×3×3×3×3×2). Clearly, generating such a plenty of models would surpass the available computational resources and produce an overwhelming amount of data that is likely unable to understand. Therefore, the parametric investigation was categorized into two groups in which the first group examined the effects of the mechanical properties of materials and cross-section dimensions by varying parameters (1)-(5), resulting in the creation of 108 models. The second group evaluated the effects of construction details with the variation of remaining parameters (6)-(9), which generated 28 models. Accordingly, a total of 136 models was generated for parametric analysis.

The 108 models in the first group of this study all shared the same construction details with s_{stud} of 100 mm, b_f of 120 mm, t_f of 8 mm (b_f/t_f = 15), t_w of 6 mm, h_w of 6 mm (h_w/t_w = 27), and an identical PSS slab. Given the expected strong influence of $f_{y,HSS}$ on the beams' flexural performance, the 108 models were subdivided into two portions with each value of $f_{y,HSS}$ for each group. Table 3 lists 54 models with an identical S690 HSS I-section, while Table 4 describes 54 models with an identical S960 HSS I-section. Although s_{stud} was consistently kept at 100 mm, variations in cross-section dimensions and mechanical properties of materials resulted a non-constant degree of shear connection (η) among these models. Accordingly, all HSS-ECC beams of the first group were partially shear connected in which η varied from 0.42 to 0.82.

To evaluate the effects of construction details in the second group, a standard cross-section of the beam with the w_{ECC} of 600 mm, t_{ECC} of 140 mm, d_{HSS} of 180 mm was adopted. The effects of s_{stud} on the bending behaviour of the HSS-ECC beam were evaluated by considering three values of s_{stud} of 75, 100 and 200 mm in combination with four pairs of material, which were defined based on a

combination of f'_{ECC} and $f_{y,HSS}$ (i.e., f'_{ECC} = 40 Mpa, $f_{y,HSS}$= 690 Mpa; f'_{ECC} = 40 Mpa, $f_{y,HSS}$= 960 Mpa; f'_{ECC} = 70 Mpa, $f_{y,HSS}$= 690 Mpa; and f'_{ECC} = 70 Mpa, $f_{y,HSS}$= 960 Mpa). The remaining construction details were kept constant with b_f/t_f of 15, h_w/t_w of 27 and PSS slab. Accordingly, eight models were created with the variation of η from 0.41 to 1.23. For examining the effect of the b_f/t_f and h_w/t_w on the bending behaviour of the HSS-ECC beam, two values of b_f/t_f (10 and 12) and two value of h_w/t_w (16 and 20) were chosen while four pairs of ECC and HSS were employed (i.e., f'_{ECC} = 40 Mpa, $f_{y,HSS}$= 690 Mpa; f'_{ECC} = 40 Mpa, $f_{y,HSS}$= 960 Mpa; f'_{ECC} = 70 Mpa, $f_{y,HSS}$= 690 Mpa; and f'_{ECC} = 70 Mpa, $f_{y,HSS}$= 960 Mpa). For evaluating the effect of b_f/t_f and h_w/t_w, the s_{stud} of 100 mm and PSS slab were adopted. Accordingly, sixteen models were generated for evaluating the effect of the b_f/t_f and h_w/t_w. The effects of ECC slab type were determined by using solid slab instead of PPS in combination of with four material properties. The other construction details with s_{stud} of 100 mm, b_f/t_f of 15 and h_w/t_w of 27 were adopted in modelling the performance of HSS-ECC beam. As a result, four models were created with s_{stud} of 100 mm, b_f/t_f of 15 and h_w/t_w of 27. Table 5 presents 28 models of HSS-ECC beam used in the second group.
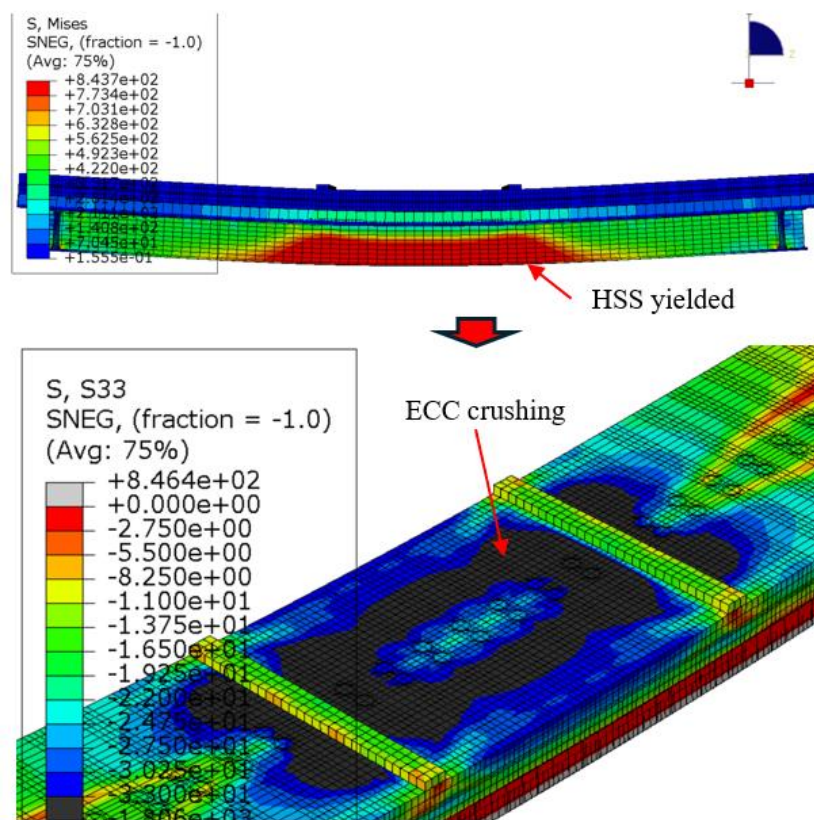

Fig. 3. Typical failure mode of HSS-ECC beam

As illustrated in Tables 3-5, the notations of HSS-ECC beams modelled in the parametric analysis consisted of five parts separated by a hyphen. Each part of notation includes two capital letters (e.g., CF) and a number (e.g., 40). The first capital letter represents the material, which is either letter C or S (C stands for ECC and S stands for high strength steel). The following capital letter represents either the cross-section dimension or strength of material in which F denotes the compressive strength/yield strength of ECC/HSS, W and T present the ECC slab width and ECC slab thickness, respectively, and D denotes the depth of HSS I-section. The number indicates the value of the cross-section dimension is in mm while MPa for material strength. For example, the CF40-CW600-CT140-SF690-SD180 beam refers to the HSS-ECC beam with the f'_{ECC} of 40 MPa, w_{ECC} of 600 mm, t_{ECC} of 140 mm, $f_{y,HSS}$ of 690 MPa and d_{HSS} of 180 mm.

4. Parametric Study Results

Parametric investigation was undertaken to evaluate the effect of key parameters [i.e., ECC compressive strength (f'_{ECC}), HSS yield strength ($f_{y,HSS}$), ECC slab width (w_{ECC}), ECC slab thickness (t_{ECC}), HSS section depth (d_{HSS}), ratio of HSS section flange width and thickness (b_f/t_f), ratio of HSS section web height and thickness (h_w/t_w), shear stud spacing (s_{stud}), and ECC slab type] on the bending behaviour of beams that is represented by three main indicators consisting of rotation capacity (R), initial bending stiffness (EI_0), and normalised bending capacity (M_{FE}/M_{ps}). M_{FE}/M_{ps} presents ratio of moment capacity of composite beam (M_{FE}) to moment capacity of HSS section alone (M_{ps}). The R of a composite beam is crucial for determining moment redistribution in plastic design. The R is computed by dividing the rotation at the ultimate moment (θ_u) by that at the yielding moment (θ_y) [24]. The R of simply supported beams adopted in this study is computed by dividing the mid-span deflection at the maximum load by the mid-span deflection at the yield load. Tables 3 and 4, respectively, present the effect of cross-section dimensions and mechanical properties of materials on the flexural strength of HSS-ECC beam while Table 5 indicates the effect of construction details on the flexural strength of HSS-ECC beam. Given that the parametric analysis encompasses 136 models; to present the findings concisely, the following sections will present the overall tendency and then focus on the effects of different parameters by presenting the results from selected beams.

Table 3. Influence of the mechanical properties of materials and cross-section dimensions on flexural strength of HSS-ECC beam with S690 HSS I-section

Beam (HSS S690 MPa)*		η	EI_0 (kN/mm)	R	M_{FE}/M_{ps}
CW600-CT140-SD180	CF40-SF690	0.82	23.11	2.32	2.36
	CF70-SF690	0.82	26.30	2.90	2.73
CW600-CT140-SD230	CF40-SF690	0.82	32.22	2.56	2.15
	CF70-SF690	0.74	35.85	3.10	2.44
CW600-CT140-SD280	CF40-SF690	0.82	43.46	2.71	2.05
	CF70-SF690	0.68	48.61	3.38	2.29
CW600-CT170-SD180	CF40-SF690	0.71	28.39	2.09	2.64
	CF70-SF690	0.82	32.34	2.60	3.18
CW600-CT170-SD230	CF40-SF690	0.64	37.60	2.10	2.37
	CF70-SF690	0.74	43.52	2.92	2.79
CW600-CT170-SD280	CF40-SF690	0.61	48.61	2.22	2.22
	CF70-SF690	0.68	55.42	3.03	2.56
CW600-CT200-SD180	CF40-SF690	0.71	33.91	1.84	3.00
	CF70-SF690	0.82	39.94	2.38	3.63
CW600-CT200-SD230	CF40-SF690	0.64	45.97	2.07	2.68
	CF70-SF690	0.74	52.45	2.57	3.20
CW600-CT200-SD280	CF40-SF690	0.59	56.08	1.91	2.41
	CF70-SF690	0.68	64.51	2.57	2.83
CW1000-CT140-SD180	CF40-SF690	0.71	26.35	2.23	2.62
	CF70-SF690	0.82	30.10	2.91	3.10
CW1000-CT140-SD230	CF40-SF690	0.64	37.01	2.72	2.40
	CF70-SF690	0.74	41.45	3.55	2.82
CW1000-CT140-SD280	CF40-SF690	0.59	48.93	3.11	2.25
	CF70-SF690	0.68	54.44	3.78	2.55
CW1000-CT170-SD180	CF40-SF690	0.71	33.23	2.04	3.05
	CF70-SF690	0.82	38.32	2.52	3.70
CW1000-CT170-SD230	CF40-SF690	0.65	44.65	2.35	2.70
	CF70-SF690	0.74	50.38	2.81	3.20

CW1000-CT170-SD280	CF40-SF690	0.59	57.13	2.89	2.51
	CF70-SF690	0.68	64.44	3.24	2.91
CW1000-CT200-SD180	CF40-SF690	0.71	39.84	1.82	3.54
	CF70-SF690	0.82	47.78	2.28	4.40
CW1000-CT200-SD230	CF40-SF690	0.65	52.77	2.00	3.15
	CF70-SF690	0.74	60.63	2.31	3.75
CW1000-CT200-SD280	CF40-SF690	0.59	66.76	2.12	2.81
	CF70-SF690	0.68	75.85	2.46	3.35
CW1400-CT140-SD180	CF40-SF690	0.71	25.51	2.65	2.97
	CF70-SF690	0.82	33.11	4.25	3.54
CW1400-CT140-SD230	CF40-SF690	0.65	38.91	2.91	2.69
	CF70-SF690	0.74	44.04	4.05	3.05
CW1400-CT140-SD280	CF40-SF690	0.59	50.64	3.01	2.50
	CF70-SF690	0.68	57.11	4.18	2.76
CW1400-CT170-SD180	CF40-SF690	0.71	36.39	2.45	3.68
	CF70-SF690	0.82	42.02	3.16	4.23
CW1400-CT170-SD230	CF40-SF690	0.65	49.05	4.18	3.08
	CF70-SF690	0.74	50.40	4.28	3.66
CW1400-CT170-SD280	CF40-SF690	0.59	59.81	4.58	2.80
	CF70-SF690	0.68	69.79	4.07	3.27
CW1400-CT200-SD180	CF40-SF690	0.71	46.06	2.59	4.50
	CF70-SF690	0.82	54.36	3.58	5.34
CW1400-CT200-SD230	CF40-SF690	0.65	57.91	2.65	3.55
	CF70-SF690	0.74	65.32	3.50	4.36
CW1400-CT200-SD280	CF40-SF690	0.59	71.90	2.77	3.33
	CF70-SF690	0.68	78.93	3.58	3.83
Mean					3.06
SD					0.67

*b_f/t_f=15 (b_f=120 mm, t_f=8 mm), t_w=6 mm, s_{stud} =100 mm, and PSS slab.

Table 4. Influence of the mechanical properties of materials and cross-section dimensions on flexural strength of HSS-ECC beam with S960 HSS I-section

Beam (HSS S960 MPa)*		η	EI_0 (kN/mm)	R	M_{FE}/M_{ps}
CW600-CT140-SD180	CF40-SF960	0.82	20.93	1.44	2.00
	CF70-SF960	0.59	25.99	2.59	2.33
CW600-CT140-SD230	CF40-SF960	0.82	28.29	1.62	1.84
	CF70-SF960	0.54	34.39	2.00	2.10
CW600-CT140-SD280	CF40-SF960	0.82	47.63	1.34	1.69
	CF70-SF960	0.54	47.04	2.16	2.02
CW600-CT170-SD180	CF40-SF960	0.61	25.99	1.34	2.15
	CF70-SF960	0.59	29.93	1.53	2.58
CW600-CT170-SD230	CF40-SF960	0.61	33.00	1.36	1.97
	CF70-SF960	0.53	40.90	1.72	2.31
CW600-CT170-SD280	CF40-SF960	0.61	45.14	1.50	1.86
	CF70-SF960	0.49	52.39	1.78	2.15
CW600-CT200-SD180	CF40-SF960	0.51	30.78	1.25	2.39
	CF70-SF960	0.59	36.37	1.44	2.89

CW600-CT200-SD230	CF40-SF960	0.48	40.54	1.26	2.18
	CF70-SF960	0.53	49.40	1.60	2.61
CW600-CT200-SD280	CF40-SF960	0.48	49.82	1.21	1.97
	CF70-SF960	0.49	59.37	1.54	2.31
CW1000-CT140-SD180	CF40-SF960	0.51	23.80	1.37	2.20
	CF70-SF960	0.59	28.41	1.76	2.55
CW1000-CT140-SD230	CF40-SF960	0.49	34.43	1.65	2.03
	CF70-SF960	0.53	39.48	2.03	2.34
CW1000-CT140-ID280	CF40-SF960	0.49	45.48	1.92	1.94
	CF70-SF960	0.49	51.85	2.20	2.19
CW1000-CT170-SD180	CF40-SF960	0.51	30.57	1.36	2.50
	CF70-SF960	0.59	35.78	2.46	2.94
CW1000-CT170-SD230	CF40-SF960	0.46	38.67	1.32	2.29
	CF70-SF960	0.53	48.13	1.71	2.61
CW1000-CT170-SD280	CF40-SF960	0.42	53.07	2.58	2.14
	CF70-SF960	0.49	61.17	1.80	2.42
CW1000-CT200-SD180	CF40-SF960	0.51	35.83	1.17	2.84
	CF70-SF960	0.59	44.69	1.47	3.48
CW1000-CT200-SD230	CF40-SF960	0.46	48.65	1.23	2.62
	CF70-SF960	0.53	55.95	1.43	3.03
CW1000-CT200-SD280	CF40-SF960	0.42	63.74	1.51	2.40
	CF70-SF960	0.49	71.96	1.67	2.76
CW1400-CT140-SD180	CF40-SF960	0.51	25.37	1.57	2.43
	CF70-SF960	0.59	30.81	2.38	2.88
CW1400-CT140-SD230	CF40-SF960	0.46	34.17	1.73	2.29
	CF70-SF960	0.53	41.88	2.59	2.54
CW1400-CT140-SD280	CF40-SF960	0.42	48.44	1.85	2.14
	CF70-SF960	0.49	54.41	2.73	2.33
CW1400-CT170-SD180	CF40-SF960	0.51	33.95	1.46	2.79
	CF70-SF960	0.59	38.44	2.11	3.40
CW1400-CT170-SD230	CF40-SF960	0.46	43.60	3.02	2.56
	CF70-SF960	0.53	52.57	3.18	2.96
CW1400-CT170-SD280	CF40-SF960	0.42	56.51	3.06	2.35
	CF70-SF960	0.49	67.13	3.24	2.68
CW1400-CT200-SD180	CF40-SF960	0.51	43.02	1.55	3.61
	CF70-SF960	0.59	49.18	2.10	4.25
CW1400-CT200-SD230	CF40-SF960	0.46	53.57	1.32	2.77
	CF70-SF960	0.53	62.98	2.35	3.57
CW1400-CT200-SD280	CF40-SF960	0.42	69.21	1.74	2.76
	CF70-SF960	0.49	77.50	2.42	3.15
Mean					2.52
SD					0.50

*b_f/t_f=15 (b_f=120 mm, t_f=8 mm), t_w=6 mm, s_{stud} =100 mm, and *PSS slab.*

Table 5. Effect of different construction details on the flexural strength of HSS-ECC beam

Beam construction details *		η	EI_0 (kN/mm)	R	M_{FE}/M_{ps}
CW600-CT140-SD180	CF40-SF690	0.41	21.29	2.51	2.27
(stud spacing = 200 mm)	CF40-SF960	0.41	23.44	3.07	2.61
PSS, b_f/t_f = 15	CF70-SF690	0.41	19.24	1.68	1.91
h_w/t_w = 27	CF70-SF960	0.29	20.26	2.13	2.21
CW600-CT140-SD180	CF40-SF690	1.23	23.40	2.32	2.36
(stud spacing = 75 mm)	CF40-SF960	1.23	25.84	2.63	2.73
PSS, b_f/t_f = 15	CF70-SF690	1.22	22.23	1.65	2.01
h_w/t_w = 27	CF70-SF960	0.88	25.38	1.89	2.33
CW600-CT140-SD180	CF40-SF690	0.82	24.95	2.16	2.12
stud spacing = 100 mm	CF40-SF960	0.82	27.60	2.56	2.46
PSS, (b_f/t_f = 12)	CF70-SF690	0.71	22.46	1.32	2.49
h_w/t_w = 27	CF70-SF960	0.54	26.50	1.75	2.90
CW600-CT140-SD180	CF40-SF690	0.82	26.05	1.94	1.95
stud spacing = 100 mm	CF40-SF960	0.82	30.05	1.96	2.25
PSS, (b_f/t_f = 10)	CF70-SF690	0.62	23.36	1.65	2.29
h_w/t_w = 27	CF70-SF960	0.54	27.85	1.54	2.65
CW600-CT140-SD180	CF40-SF690	0.82	25.73	1.97	2.16
stud spacing = 100 mm	CF40-SF960	0.82	29.71	2.54	2.51
PSS, b_f/t_f = 15	CF70-SF690	0.64	23.55	1.33	2.52
(h_w/t_w= 20)	CF70-SF960	0.54	27.74	1.59	2.94
CW600-CT140-SD180	CF40-SF690	0.82	26.80	1.86	2.20
stud spacing = 100 mm	CF40-SF960	0.82	30.60	2.34	2.56
PSS, b_f/t_f = 15	CF70-SF690	0.59	23.77	1.22	2.52
(h_w/t_w= 16)	CF70-SF960	0.54	28.49	1.47	2.95
CW600-CT140-SD180	CF40-SF690	0.71	23.11	2.32	2.36
stud spacing = 100 mm	CF40-SF960	0.81	26.30	2.90	2.73
(solid slab), b_f/t_f = 15	CF70-SF690	0.51	20.93	1.44	2.00
h_w/t_w = 27	CF70-SF960	0.59	25.99	2.59	2.33
Mean					2.40
SD					0.29

* The bold words/symbols inside brackets show the variation of construction details.

4.1. Overall Tendency

To better understand the overall tendency of initial stiffness and bending capacity (M_{FE}/M_{ps}), their values for all composite beam models of different material properties and beam configurations are plotted in Figures 4 and 5. It is exhibited in Figure 4 that initial stiffness is significantly increased with the increase in beam cross-section dimensions including HSS section depth, ECC slab width and thickness. It is also worth noting that group with higher ECC compressive strength (group 70-690 and 70-960) show much higher intial stiffness. For M_{FE}/M_{ps} shown in Figure 5, it is indicated that in the same group of material properties, M_{FE}/M_{ps} decreases with the rise in HSS section depth but increases with the increase of ECC slab thickness and width. In all four groups of material properties, beams with ECC of 70 Mpa compressive strength and 690 Mpa HSS tensile strength (group 70-690) show highest normalized bending capacity while the least accounting for the 40-960 group.
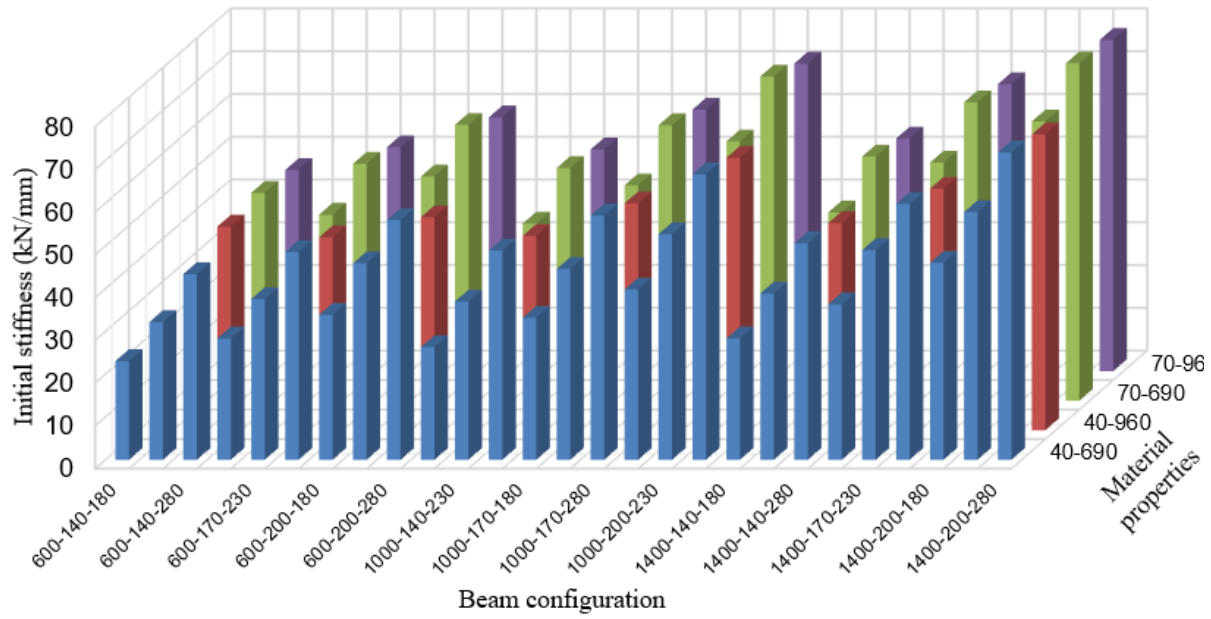
Fig. 4. Variation of initial stiffness for different material properties and beam configurations
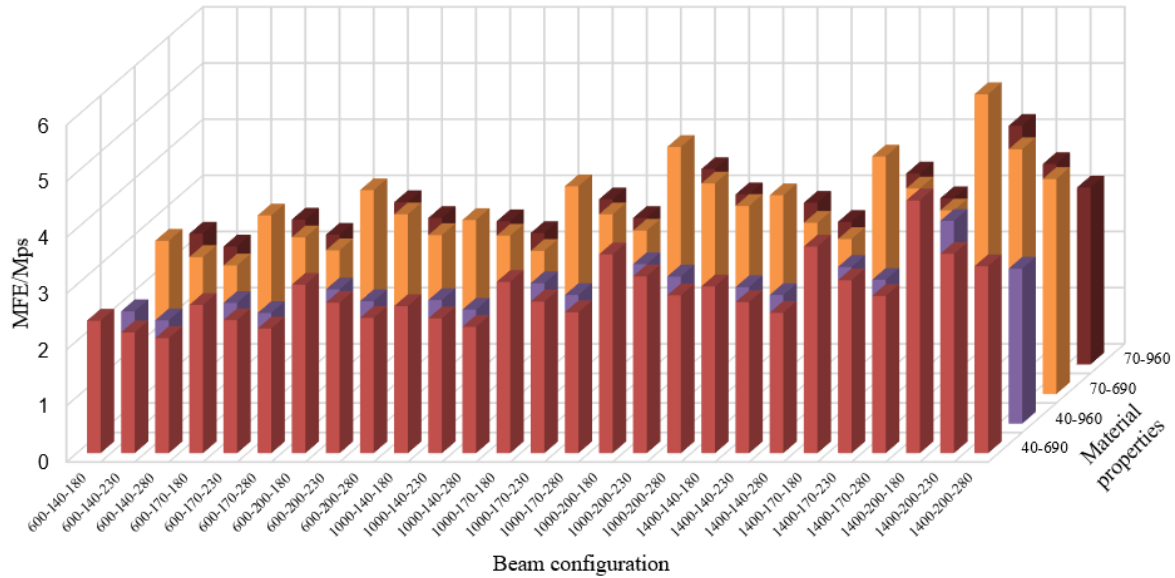

Fig. 5. Variation of M_{FE}/M_{ps} for different material properties and beam configurations

4.2. Effect of ECC compressive strength (f'_{ECC}) and HSS yield strength ($f_{y,HSS}$)

4.2.1 Initial Bending Stiffness (EI_0)

Figure 6 illustrates the $P-\delta$ relationship for two typical HSS-ECC beams (e.g., CW600-CT140-SD180 and CW600-CT200-SD230) having the variation of f'_{ECC} and $f_{y,HSS}$. Figure 7(a) compares the effects of mechanical properties of materials on the EI_0. The data reveals that EI_0 is highly sensitive to f'_{ECC}. For instance, in the CW600-CT140-SD180 Beam, increasing f'_{ECC} from 40 MPa to 70 MPa resulted in a 12% increase in EI_0, from 23.62 kN/mm to 26.52 kN/mm, as shown in Figures 6(a) and 7(a). Similarly, the CW600-CT200-SD230 Beam experienced the same 12% increase in EI_0 [Figures 7(b) and 7(a)]. Also, Figures 6 and 7(a) indicate that EI_0 is not significantly affected by $f_{y,HSS}$, as beams with identical f'_{ECC} but different $f_{y,HSS}$ exhibited the same EI_0. This can be attributed to the fact that EI_0 is influenced by the elastic modulus of beam's material properties. It is clear that ECC with higher f'_{ECC} has a higher elastic modulus (Table 2), while the Young's modulus of HSS remains consistent across different grades.
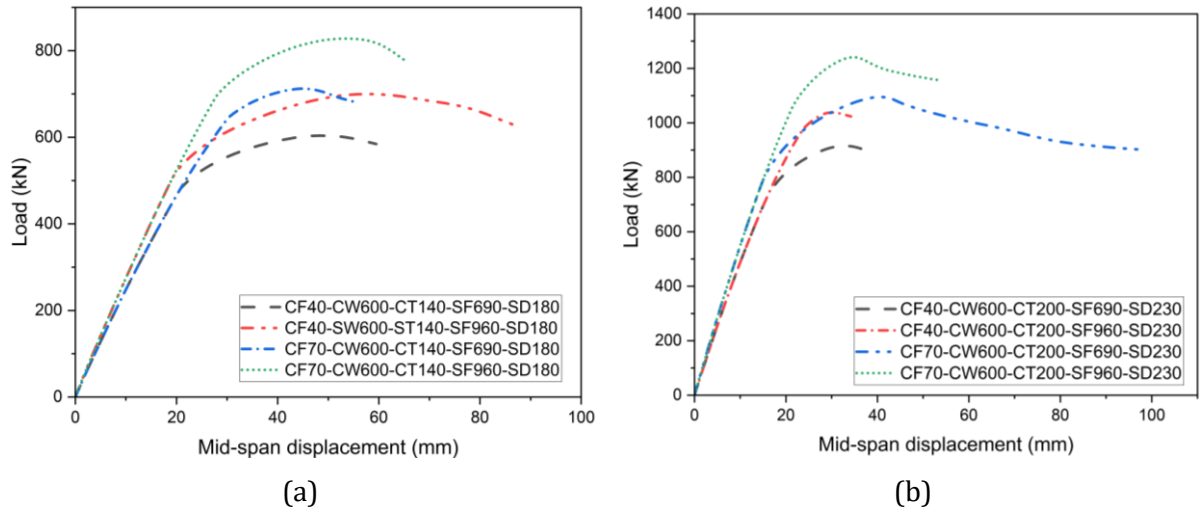
Fig. 6. $P - \delta$ relationship of HSS-ECC beam with various f'_{ECC} and $f_{y,HSS}$. (a) CW600-CT140-SD180 Beam; (b) CW600-CT200-SD230 Beam
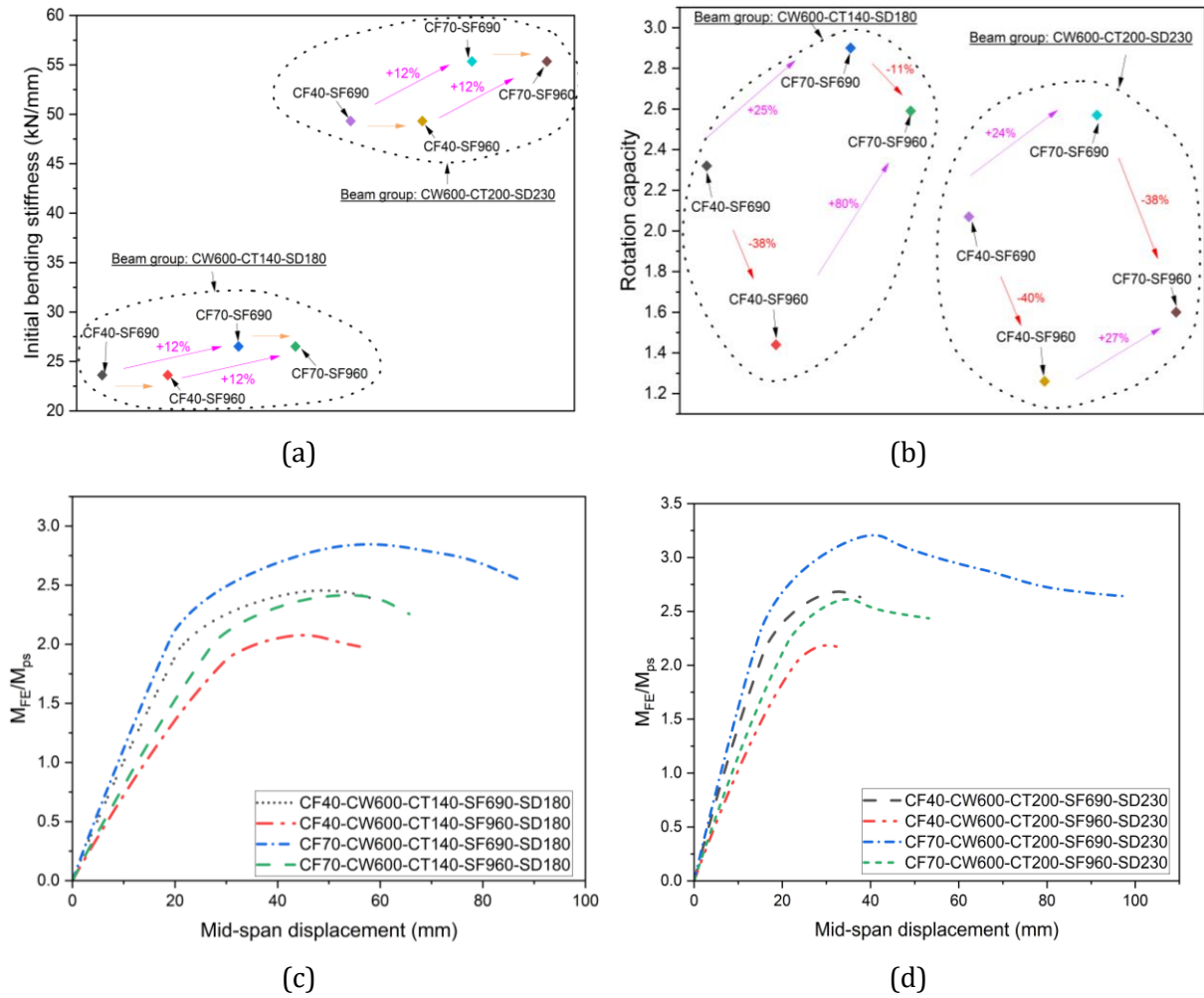

Fig. 7. Effect of f'_{ECC} and $f_{y,HSS}$ on flexural strength of HSS-ECC beam: (a) Initial bending stiffness; (b) Rotation capacity; (c) and (d) Normalized bending capacity

4.2.2 Rotation Capacity (R)

The effect of mechanical properties of constitutive materials on R for two typical HSS-ECC beams (e.g., CW600-CT140-SD180 and CW600-CT200-SD230) is depicted in Figure 7(b). When f'_{ECC} changed from 40 MPa to 70 MPa, R for the CW600-CT140-SD180 Beam with S690 HSS I-section obtained an increase by 25%, from 2.32 to 2.90. For S960 HSS I-section, this increase was even more pronounced, with an 80% rise from 1.44 to 2.59. A similar pattern was observed for the CW600-CT200-SD230 Beam in which R obtained an increase by 24% for S690 HSS I-sections and 27% for S960 HSS I-sections. Regarding the effects of $f_{y,HSS}$, an increase in $f_{y,HSS}$ resulted in a decrease in R. It can be seen in Figure 7(b) that, for the CW600-CT140-SD180 Beam with 40 MPa ECC, increasing $f_{y,HSS}$ from 690 MPa to 960 MPa led to a 38% reduction in R, from 2.32 to 1.44, and an 11% reduction, from 2.9 to 2.59 for a similar beam with 70 MPa ECC. A similar trend was noted for the CW600-CT200-SD230 Beam with 40 MPa ECC, R decreased by 40% when $f_{y,HSS}$ changed from 690 MPa to 960 MPa, and by 38% when the ECC had the f'_{ECC} of 70 MPa.

4.2.3 Bending Capacity (M_{FE}/M_{ps})

The effect of mechanical properties of constitutive materials on the HSS-ECC beam bending capacity can be represented by the normalized moment capacity M_{FE}/M_{ps}, where M_{FE} is the HSS-ECC beam's moment capacity (determined through FE modelling) and M_{ps} is the HSS I-section's full plastic moment capacity. Figures 7(c) and 7(d) display typical plots of M_{FE}/M_{ps} versus δ for the CW600-CT140-SD180 and CW600-CT200-SD230 Beams. As shown in Figure 5(c), increasing f'_{ECC} from 40 MPa to 70 MPa resulted in a 15.6% increase in M_{FE}/M_{ps} (from 2.43 to 2.81) for the S690 HSS section and a 13.8% increase (from 2.10 to 2.39) for S960 HSS beams. For the CW600-CT200-SD230 Beam, a 20% increase in M_{FE}/M_{ps} was observed for both steel grades. This increase is attributed to the upward shift of the plastic neutral axis (PNA) towards the ECC slab top surface when f'_{ECC} is increased, which lengthens the moment lever arm between the HSS section and the ECC slab, thus enhancing the bending capacity. Regarding the effect of $f_{y,HSS}$, Figures 7(c), (d) indicate that M_{FE}/M_{ps} reduced as $f_{y,HSS}$ changed from 690 MPa to 960 MPa. This is because as $f_{y,HSS}$ increases, the term M_{ps} rises proportionally. However, in the HSS-ECC beam, the PNA shifts closer to the bottom of the beam and reduces the lever arm length. Consequently, although M_{FE} increased, the rate of increase was lower than that of M_{ps}, resulting in a decreased M_{FE}/M_{ps} ratio.

4.3. ECC slab width (w_{ECC}) effect

4.3.1 Initial Bending Stiffness (EI_0)

Figure 8 presents the $P - δ$ curves for two typical HSS-ECC beams (e.g., CF40-CT140-SF690-SD180 and CF40-CT140-SF690-SD230) with variation of w_{ECC},. Figure 9(a) compares their EI_0, showing that EI_0 increases with the increase of w_{ECC}.
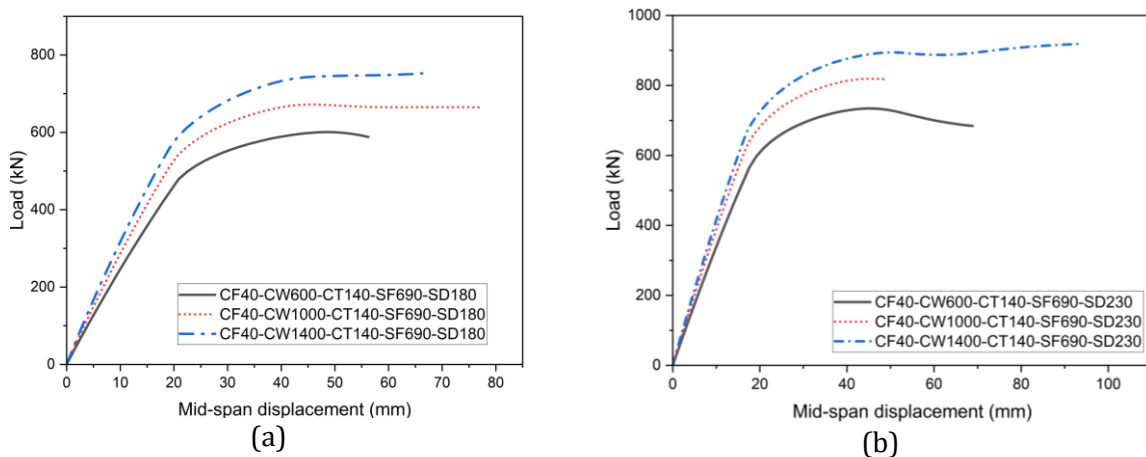

Fig. 8. Effect of w_{ECC} on $P - δ$ relationship: (a) CF40-CT140-SF690-SD180 Beam; (b) CF40-CT140-SF690-SD230 Beam

Specifically, for the CF40-CT140-SF690-SD180 Beam, increasing the w_{ECC} from 600 mm to 1000 mm and 1400 mm resulted in EI_0 increase of 17% and 34%, respectively. A similar trend is observed for the CF40-CT140-SF690-SD230 Beam.
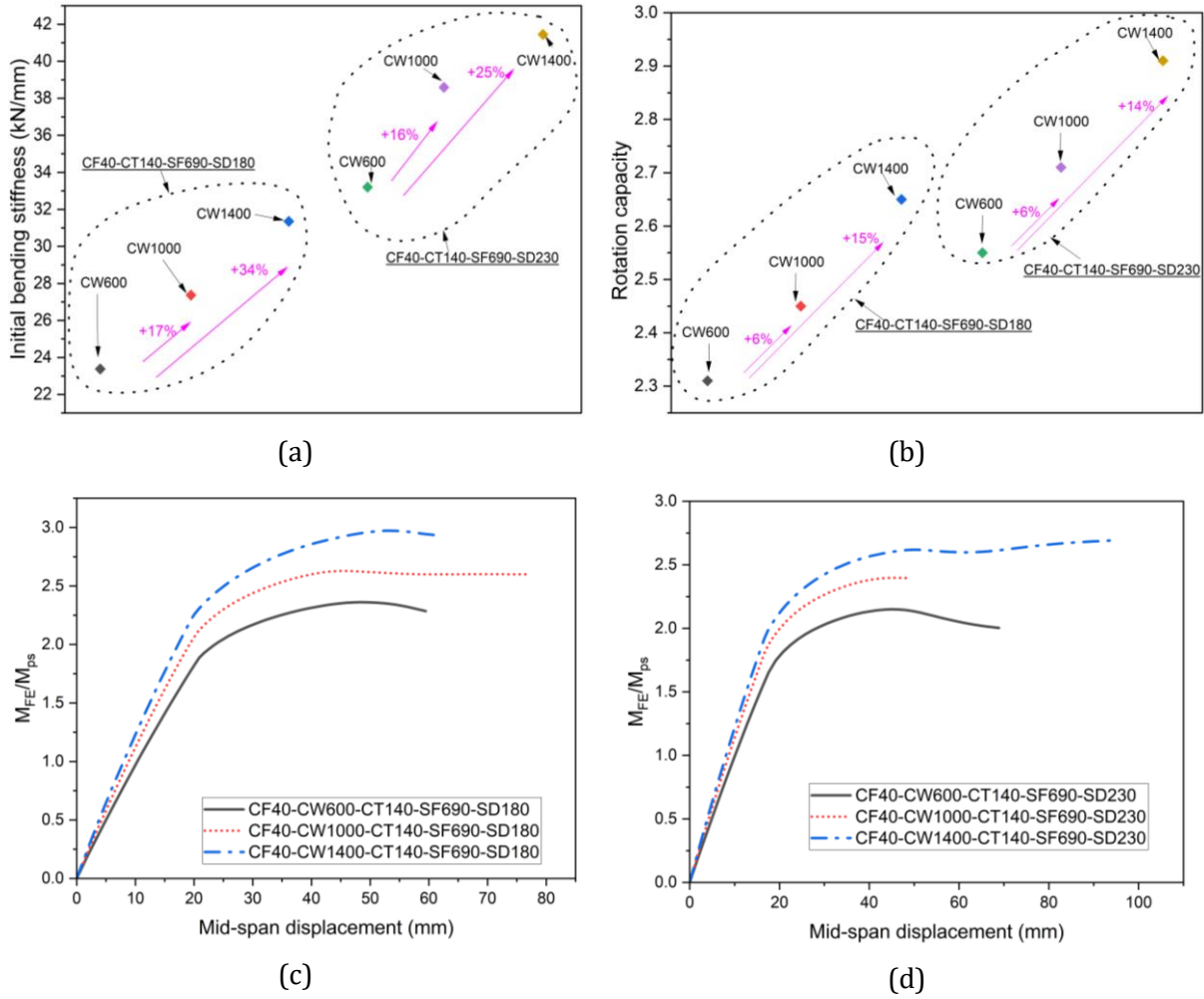

Fig. 9. Effect of w_{ECC} on flexural strength of HSS-ECC beam: (a) Initial bending stiffness; (b) Rotation capacity; (c) and (d) Normalized bending capacity

4.3.2 Rotation Capacity (R)

Figure 9(b) illustrates the impact of w_{ECC} on R for the same beams. Increasing w_{ECC} from 600 mm to 1000 mm and 1400 mm led to a 6% and 15% rise in R, respectively. This is because a wider slab shifts the plastic neutral axis (PNA) upwards, leading to a smaller strain value at the slab's top surface and delaying its crushing, allowing for greater rotation capacity.

4.3.3 Bending Capacity (M_{FE}/M_{ps})

Regarding bending strength capacity, Figures 9(c) and 9(d) show that increasing w_{ECC} from 600 mm to 1000 mm and 1400 mm led to approximately a 15% and 30% increase in M_{FE}/M_{ps}, respectively. This tendency is also due to the upward shift of the PNA, which lengthens the moment lever arm.

4.4. ECC Slab Thickness (t_{ECC}) Effect

4.4.1 Initial Bending Stiffness (EI_0)

Figures 10(a) and 10(b) depict the $P - \delta$ curves for two typical HSS-ECC beams (e.g., CF40-CW600-SF690-SD180 and CF70-CW1000-SF690-SD230) with a variation of t_{ECC}, showing that EI_0 increases with the rise of t_{ECC}. According to Figure 9(a), increasing t_{ECC} from 140 mm to 170 mm

and 200 mm resulted in a 28% and 57% increase in EI_0, respectively. This increase is clearly because of the greater resistance offered by a larger slab section.
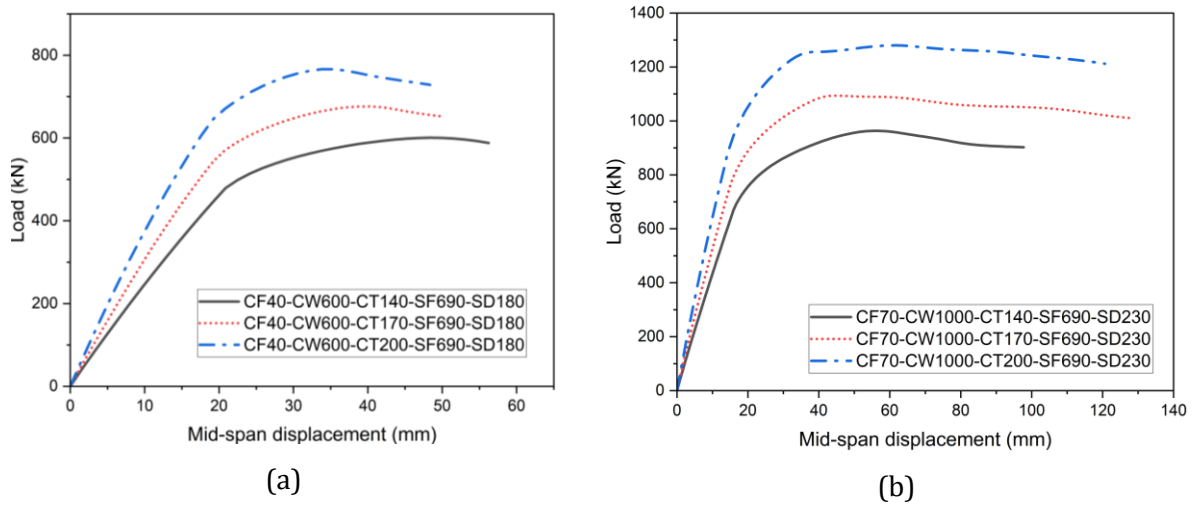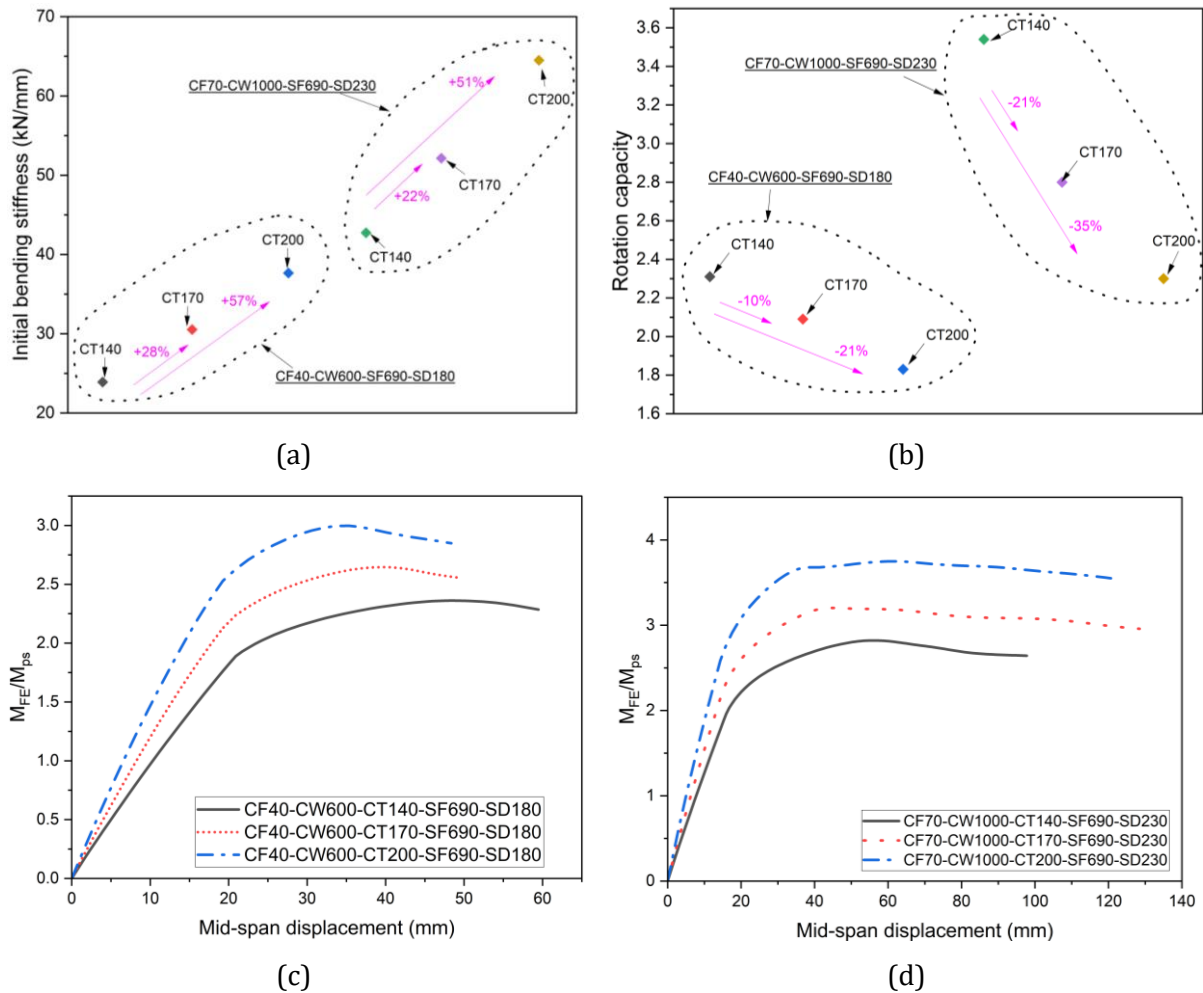

(a)   (b)

Fig. 10. Effect of t_{ECC} on $P - \delta$ relationship: (a) CF40-CW600-SF690-SD180 Beam; (b) CF70-CW1000-SF690-SD230 Beam

(a)   (b)

(c)   (d)

Fig. 11. Effect of t_{ECC} on flexural strength of HSS-ECC beam: (a) Initial bending stiffness; (b) Rotation capacity; (c) and (d) Normalized bending capacity

4.4.2 Rotation Capacity (R)

Figure 11(b) shows that increasing t_{ECC} decreases R. Specifically, for the CF40-CW600-SF690-SD180 Beam, increasing t_{ECC} from 140 mm to 170 mm and 200 mm resulted in R reductions of 10% and 21%, respectively. For the CF70-CW1000-SF690-SD230 Beam, the reductions were even greater, at 21% and 35%. This is because a thicker slab increases the distance between the PNA and the top surface of the slab, leading to higher compressive strain at the top surface and causing the ECC to crush at a lower rotation capacity.

4.4.3 Bending Capacity (M_{FE}/M_{ps})

Figures 11(c) and 11(d) illustrate the effects of t_{ECC} on M_{FE}/M_{ps} for two typical beams. As expected, with the HSS section and M_{ps} unchanged, M_{FE}/M_{ps} increased with t_{ECC}. This is because a thicker slab results in a longer lever arm and greater bending resistance.

4.5. Effect of HSS section depth (d_{HSS})

4.5.1 Initial Bending Stiffness (EI_0)

Figures 12(a) and (b) display the $P - \delta$ curves for beams with different d_{HSS}, indicating that EI_0 increases with d_{HSS}. Figure 13(a) further demonstrates that increasing the d_{HSS} from 180 mm to 280 mm nearly doubled the EI_0 value. This outcome is expected as a deeper HSS I-section increases the moment of inertia, resulting in higher EI_0.
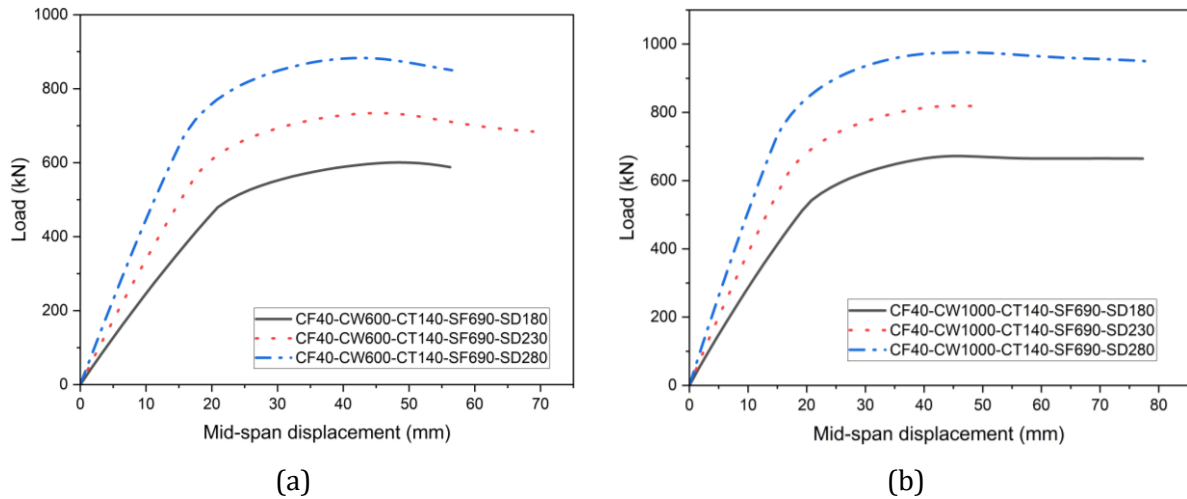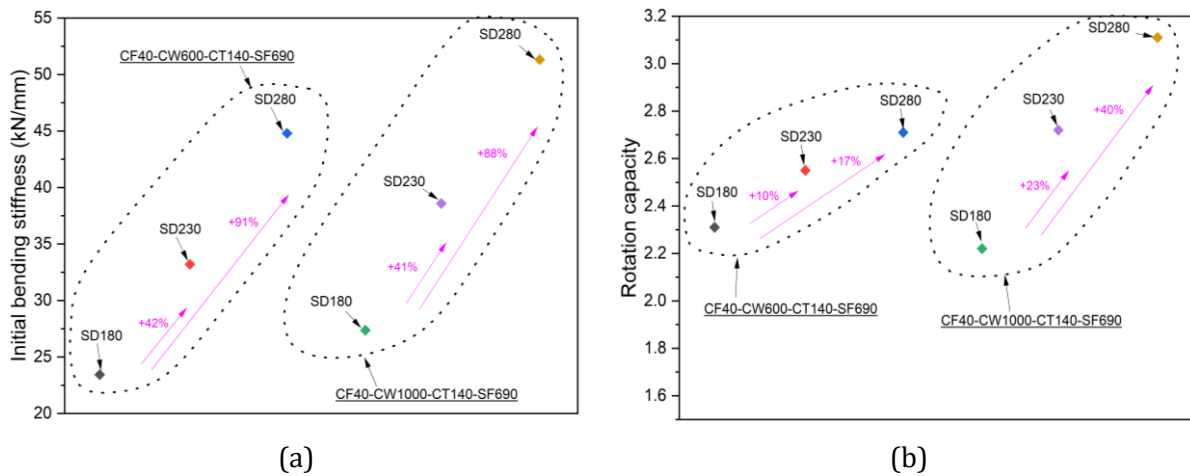

(a)   (b)

Fig. 12. Effect of d_{HSS} on $P - \delta$ relationship: (a) CF40-CW600-CT140-SF690 Beam; (b) CF40-CW1000-ST140-SF690 Beam

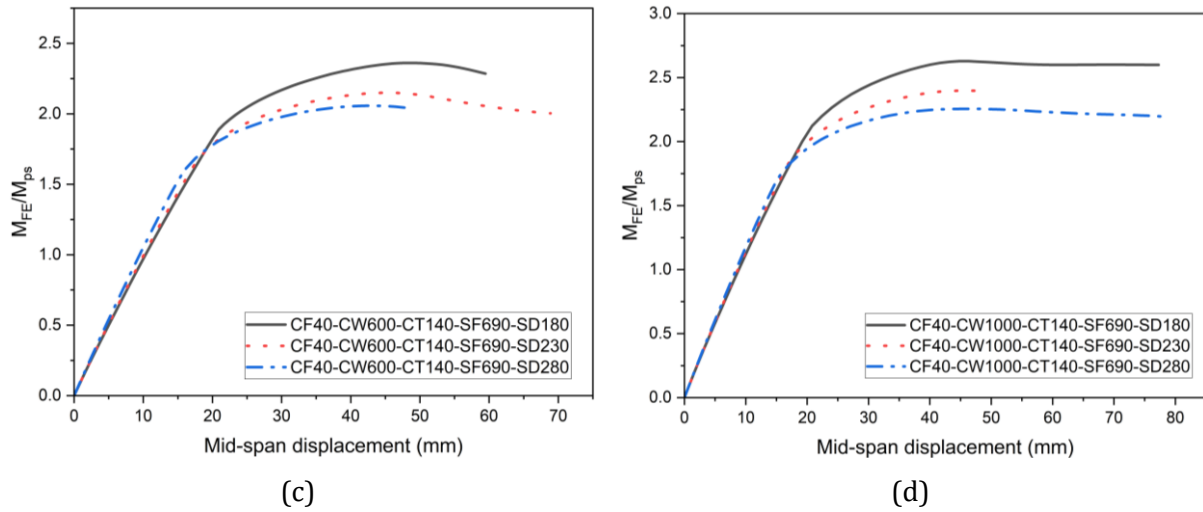(a)   (b)

Fig. 13. Effect of d_{HSS} on flexural strength of HSS-ECC beam: (a) Initial bending stiffness; (b) Rotation capacity; (c) and (d) Normalized bending capacity

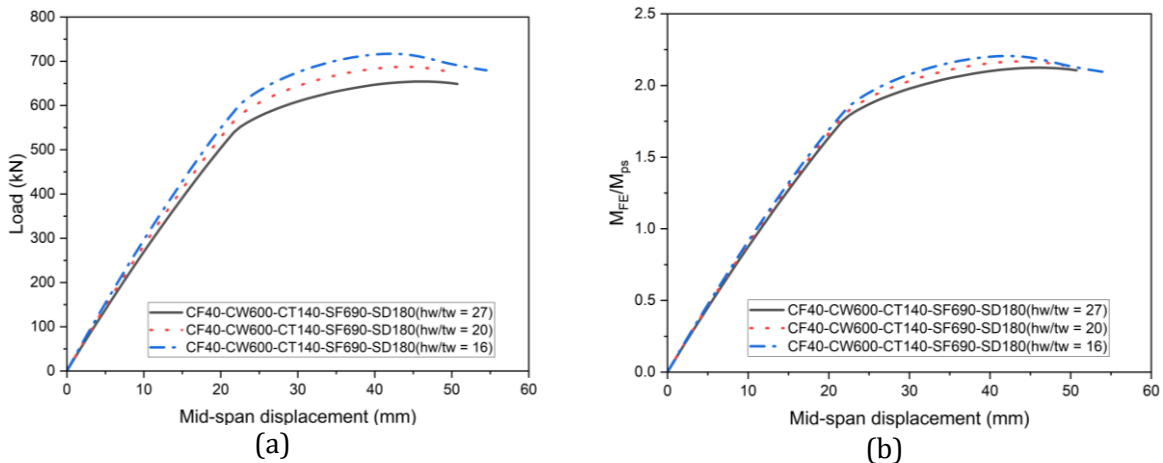### 4.5.2 Rotation Capacity (R)

Figure 13(b) shows that for the CF40-CW600-CT140-SF690 Beam, R experienced an increase by 10% and 17%, respectively, when d_{HSS} varied from 180 mm to 230 mm and 280 mm. Similar trends were observed for the CF40-CW1000-CT140-SF690 Beam in which R obtained an increase by approximately 23% and 40%.

4.5.3 Bending Capacity (M_{FE}/M_{ps})

Figures 13(c) and 13(d) present the M_{FE}/M_{ps} versus δ for beams with different values of d_{HSS}. These figures indicate that increasing d_{HSS} from 180 mm to 280 mm resulted in a 12% decrease in M_{FE}/M_{ps}. This is similar to the effect of increasing $f_{y,HSS}$, where M_{FE} increased but at a lower rate than M_{ps}. A deeper HSS section moves the PNA towards the HSS section, which reduces the tensile stress within it and thereby lowers the increased rate of M_{FE}.

4.6. HSS Section Web Height to Web Thickness Ratio (h_w/t_w) Effect

To study the effect of h_w/t_w, t_w was changed from 6 mm to 8 mm and 10 mm while h_w remained constant at 164 mm (Table 5). Figures 14(a) and 14(b) indicate the curves of M_{FE}/M_{ps} and bending capacity versus deflection δ. As h_w/t_w decreased, both M_{FE}/M_{ps} and bending capacity increased because a thicker t_w, mainly under tension, enhanced bending capacity. For EI_0, Figure 14(c) shows a small increase of 11% as t_w varied from 6 mm to 10 mm. However, Figure 14(d) reveals that R decreased by 14%. This is because a thicker web moved the PNA closer to the bottom of the beam, increasing ECC compressive strain at the top surface, leading to earlier ECC slab crushing and thus reducing R.
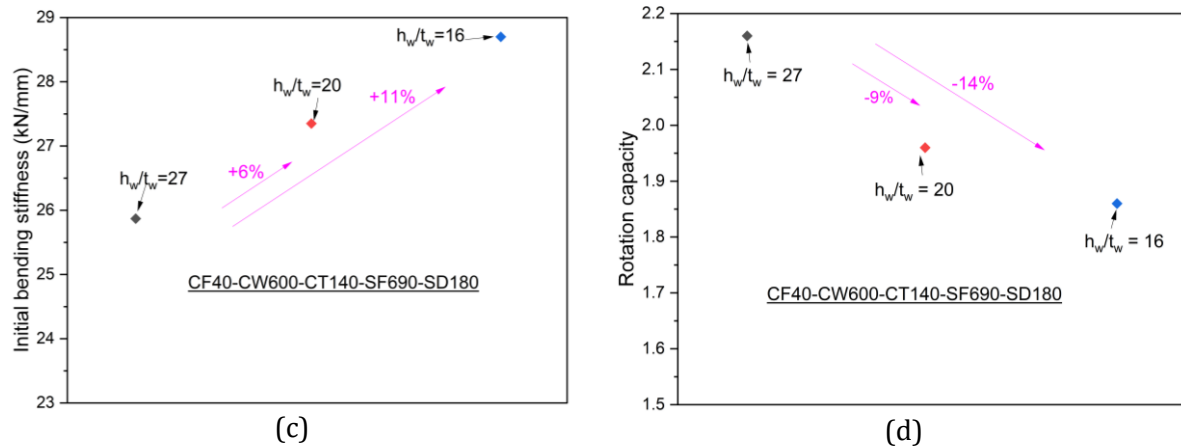
Fig. 14. Effect of h_w/t_w on flexural strength of HSS-ECC beam: (a) Load carrying capacity; (b) Normalised bending moment capacity; (c) Initial bending stiffness; (d) Rotation capacity

## 4.7. HSS Section Flange Width and Flange Thickness (b_f/t_f) Effect

The effects of the b_f/t_f were examined by changing t_f (8, 10, and 12 mm) while keeping b_f constant at 120 mm. By increasing t_f from 8 mm to 10 mm and 12 mm, respectively, the EI_0 experienced an increase by 9% and 18%, as shown in Figure 15(a). Similar to the case of h_w/t_w effect, increasing t_f resulted in a decrease in R (Figure 15(b)). Additionally, although the load-carrying capacity increased [Figure 15(c)], M_{FE}/M_{ps} decreased as t_f increased [Figure 15(d)]. This is because increasing t_f quickly raises M_{ps}, while the PNA shifts closer to the HSS section top flange, leading to the reduction of HSS section contribution to the composite beam's overall flexural resistance. Consequently, M_{FE} increased at a lower rate than M_{ps}. This suggests that a more effective way to increase M_{FE}/M_{ps} is to increase only the HSS flange thickness at the bottom.

4.8. Slab Type Effect

Solid slab is often considered as an alternative to profiled steel sheeting (PSS). A study was conducted to assess its influence on composite beams' flexural behavior. Two sets of beams having identical cross-section dimensions and mechanical properties of materials were modelled, one using a solid slab (refer to Table 5) and the other employing PSS. Figure 16 illustrates that HSS-ECC beams having solid slab and those having PSS exhibited nearly identical behaviors. Therefore, it is observed that the type of slab has marginal impact on the bending behavior of HSS-ECC beams.

4.9. Shear Stud Spacing/Shear Connection Degree Effect

Three values of s_{stud} including 75 mm, 100 mm, and 200 mm were utilized for the CW600-CT140-SD180 Beam to examine the influence of shear connection degree (η) and shear stud spacing (s_{stud}) on the beams' bending behaviour. The results depicted in Figure 17 demonstrate that beams with smaller s_{stud} (resulting in higher η) generally exhibited greater EI_0 and M_{FE}/M_{ps}, but a smaller R.
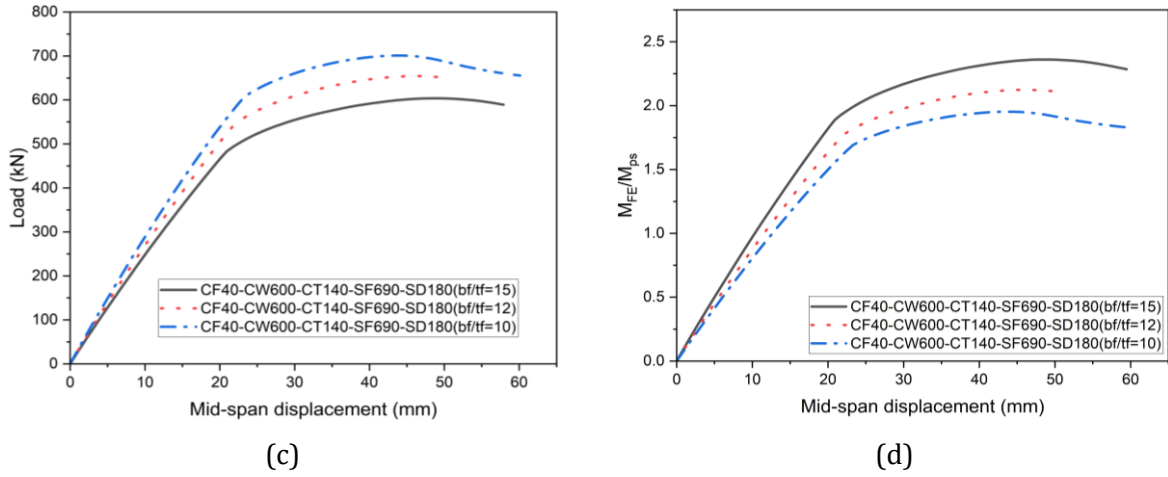

(a)

(b)

(c)   (d)
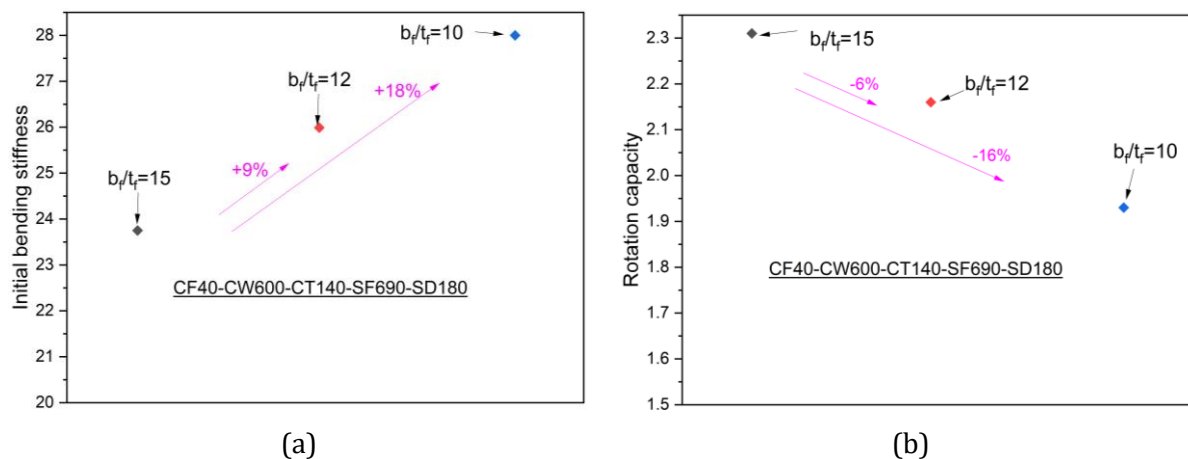
Fig. 15. Effect of b_f/t_f on flexural strength of HSS-ECC beam: (a) Initial bending stiffness; (b) Rotation capacity; (c) Load carrying capacity; (d) Normalised bending moment capacity
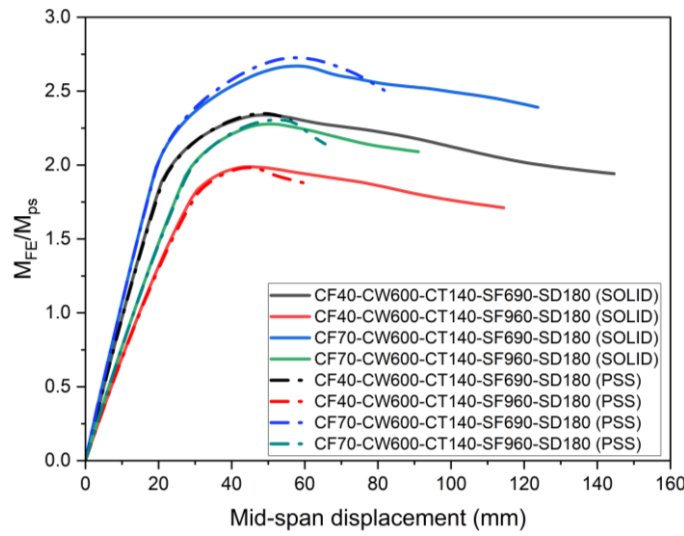

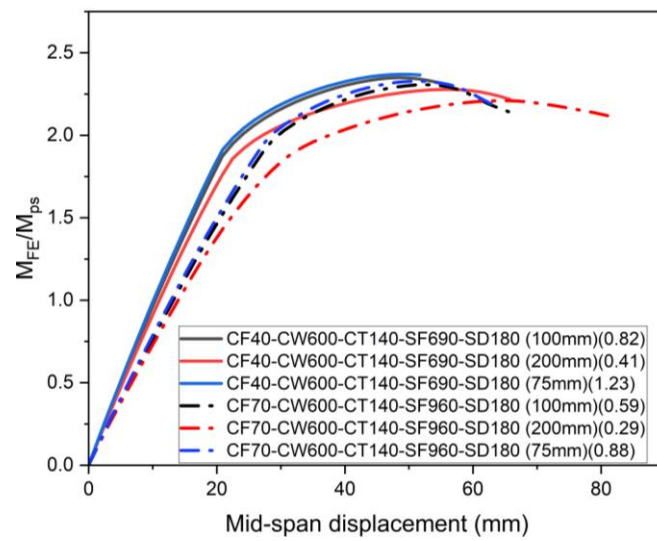Fig. 16. Effect of slab types on M_{FE}/M_{ps} of HSS-ECC beams

Fig. 17. Effect of shear stud spacing/degree of shear connection (η) on M_{FE}/M_{ps} of HSS-ECC beam. The number in the legend in the first bracket followed by mm is the value of s_{stud} and the number in the second bracket is the value of η

Figure 17 also illustrates that beams with s_{stud} of 75 mm and 100 mm exhibited similar bending behaviors because they shared a comparable degree of η. For instance, for CF40-SF690 Beam, s_{stud} of 100 mm resulted in η = 0.82, which is close to unity, indicating near-full shear connection. Thus, reducing s_{stud} to 75 mm and achieving full shear connection, beams' behaviour is almost similar. As anticipated, beams with s_{stud} of 200 mm showed significant differences compared to those with s_{stud} of 75 mm due to a substantially lower shear connection degree.

5. Conclusions

This paper thoroughly examined the effect of various parameters, categorized into three groups: mechanical properties of materials, cross-section dimensions, and construction details, on the bending behavior composite beams made of high strength steel (HSS) girder and engineered cementitious composites (ECC) slab through a parametric investigation. The bending behavior of 136 HSS-ECC composite beams was simulated using a validated nonlinear finite element (FE) model. The bending performance was assessed based on three indicators, including initial bending stiffness, rotation capacity, and flexural strength. The following concluding remarks can be given according to the parametric analysis results:

- The initial bending stiffness of HSS-ECC beam can be substantially improved to more than 50% by increasing the compressive strength of ECC, ECC slab width and ECC slab thickness as well as HSS section depth. However, the increase in HSS section web height to web thickness ratio, HSS section flange width to flange thickness ratio and shear stud spacing led to a considerable decrease in the initial bending stiffness of HSS-ECC beam. The influences of the HSS tensile strength and ECC slab type were found to be negligible.
- For rotation capacity, it was found that the increase in the compressive strength of ECC material, ECC slab width, HSS section depth, HSS section flange width to flange thickness ratio, HSS section web height to web thickness ratio and shear stud spacing resulted in a substantial enhancement in the rotation capacity of HSS-ECC beam. In contrast, the increase in the HSS yield strength, ECC slab thickness led to a significant decrease in the rotation capacity of the HSS-ECC beam. It was found that ECC slab type had almost no effect on the HSS-ECC beam's rotation capacity.
- For normalized bending moment capacity, it can be substantially enhanced by increasing the material property and dimensions of ECC slab (i.e., compressive strength, slab width and slab thickness). In contrast, the increase in the material property and dimensions of HSS section (i.e., tensile strength, section depth, section web height to web thickness ratio) led to a significant decrease in the normalized bending moment capacity of HSS-ECC beams. On the other hand, the increase of section flange width to flange thickness ratio and shear stud spacing resulted in the rise of the normalized bending moment capacity. In all four groups of material properties, beams with ECC of 70 MPa compressive strength and 690 MPa HSS tensile strength (group 70-690) show highest normalized bending capacity while the least accounting for the 40-960 group.

References

[1] Uy B. Stability and ductility of high-performance steel sections with concrete infill. Journal of Constructional Steel Research, 2008, 64(7-8): 748-754. https://doi.org/10.1016/j.jcsr.2008.01.036

[2] Kim C. S., Park H. G., Chung K. S., and Choi I. R. Eccentric axial load capacity of high-strength steel-concrete composite columns of various sectional shapes. Journal of Structural Engineering, 2014, 140(4): 04013091.3. https://doi.org/10.1061/(ASCE)ST.1943-541X.0000879

[3] Khan M. K. I., Rana M. M., Zhang Y., and Lee C. K. Behaviour of engineered cementitious composite-encased stub concrete columns under axial compression. Magazine of Concrete Research, 2020, 72(19): 984-1005. https://doi.org/10.1680/jmacr.19.00111

[4] Sheta A., Ma X., Zhuge Y., ElGawady M., Mills J. E., & Abd-Elaal E. Axial compressive behaviour of thin-walled composite columns comprise high-strength cold-formed steel and PE-ECC. Thin-Walled Structures, 2023, 184: 110471. https://doi.org/10.1016/j.tws.2022.110471

[5] Shi G., Zhou W., Bai Y., and Lin C. Local buckling of 460 MPa high strength steel welded section stub columns under axial compression. Journal of Constructional Steel Research, 2014, 100: 60-70. https://doi.org/10.1016/j.jcsr.2014.04.027

[6] Shi G., Ban H., and Bijlaard F.S.K. Tests and numerical study of ultra-high strength steel columns with end restraints. Journal of Constructional Steel Research, 2012, 70: 236-247. https://doi.org/10.1016/j.jcsr.2011.10.027

[7] Shi G., Zhou W., and Lin C. Experimental investigation on the local buckling behavior of 960 MPa high strength steel welded section stub columns. Advances in Structural Engineering, 2015, 18. https://doi.org/10.1260/1369-4332.18.3.423

[8] Shi G., Xu K., Ban H., and Lin C. Local buckling behavior of welded stub columns with normal and high strength steels. Journal of Constructional Steel Research, 2016, 119: 144-153.9. https://doi.org/10.1016/j.jcsr.2015.12.020

[9] Ban H., Shi G., Shi Y., and Bradford M. A. Experimental investigation of the overall buckling behaviour of 960 MPa high strength steel columns. Journal of Constructional Steel Research, 2013, 88: 256-266. https://doi.org/10.1016/j.jcsr.2013.05.015

[10] Rasmussen K. and Hancock G. Tests of high strength steel columns. Journal of Constructional Steel Research, 1995, 34: 27-52. https://doi.org/10.1016/0143-974X(95)97296-A

[11] Jixiang X. and Zhang Y. Seismic performance of the extended end-plate high-strength steel beam-to-column connections after fire. Structures. 2024, 70. https://doi.org/10.1016/j.istruc.2024.107786

[12] Fangxin H. and Wang Z. Cyclic behavior of high-strength steel beam-to-column welded flange-bolted web connections. Thin-Walled Structures, 2024, 201: 111999. https://doi.org/10.1016/j.tws.2024.111999

[13] Coelho A.M.G. and Bijlaard F.S. Experimental behaviour of high strength steel end-plate connections. Journal of Constructional Steel Research, 2007, 63(9): 1228-1240. https://doi.org/10.1016/j.jcsr.2006.11.010

[14] Jiang S., Shi G., Zhang N., Hou L., and Zhao H. Experimental study on seismic behavior of high strength steel flange-plate connections with box columns. Thin-Walled Structures, 2024, 194: 111285. https://doi.org/10.1016/j.tws.2023.111285

[15] Jiang S., Shi G., Zhang N., Zhao H., and Sun T. Experimental study on seismic behavior of cover-plate connections between steel beams and high strength steel box columns. Thin-Walled Structures, 2023, 193: 111208. https://doi.org/10.1016/j.tws.2023.111208

[16] Kabir, M.I., et al., Flexural behaviour of ECC-LWC encased slender high strength steel composite beams. Journal of Constructional Steel Research, 2020. 173: p. 106253. https://doi.org/10.1016/j.jcsr.2020.106253

17. Kabir, M.I., et al., Strength enhancement of high strength steel beams by engineered cementitous composite encasement. Engineering Strength, 2020. 207 p. 110288. https://doi.org/10.1016/j.engstruct.2020.110288

[18] Liu Z., Zhang,Y., Wang X., Chen Z., Xue J., and Ren B. Experimental study on the flexural response of UHPC beams encased high-strength section steel. Engineering Structures, 2025, 336: 120466. https://doi.org/10.1016/j.engstruct.2025.120466

[19] Hao N., Yang Y., Xue Y., Xu L., Feng S., Yu Y., and Huang B. Shear performance of partially encased composite beams with high-strength steel and UHPC. Journal of Constructional Steel Research, 2023, 211: 108217. https://doi.org/10.1016/j.jcsr.2023.108217

[20] Uy, B. and R. Sloane, Behavior of composite tee beams constructed with high strength steel. Journal of Constructional Steel Research, 1998, 1: 203-204. https://doi.org/10.1016/S0143-974X(98)00126-6

[21] Zhao H. and Yuan Y. Experimental studies on composite beams with high-strength steel and concrete. Steel and Composite Structures, 2010, 10(5): 373-383. https://doi.org/10.12989/scs.2010.10.5.373

[22] Ban H. and Bradford M.A. Flexural behaviour of composite beams with high strength steel. Engineering Structures, 2013, 56: 1130-1141. https://doi.org/10.1016/j.engstruct.2013.06.040

[23] Shamass R. and Cashell K.A. Behaviour of Composite Beams Made Using High Strength Steel. Structures, 2017, 12: 88-101. https://doi.org/10.1016/j.istruc.2017.08.005

[24] Ban H., Bradford M. A., Uy B., and Liu X. Available rotation capacity of composite beams with high-strength materials under sagging moment. Journal of Constructional Steel Research, 2016, 118: 156-168. https://doi.org/10.1016/j.jcsr.2015.11.008

[25] Ban H. and Bradford M.A. Elastoplastic cross-sectional behavior of composite beams with high-strength steel: analytical modeling. Journal of Structural Engineering, 2015, 141(10): 04014236. https://doi.org/10.1061/(ASCE)ST.1943-541X.0001208

[26] Jun S.-C., Lee C.-H., Han K.-H., and Kim J.-W. Flexural behavior of high-strength steel hybrid composite beams. Journal of Constructional Steel Research, 2018, 149: 269-281. https://doi.org/10.1016/j.jcsr.2018.07.020

[27] Nguyen C.-L. and Lee C.-K. Experimental study of flexural behaviour of high strength steel (HSS) - Engineered Cementitious Composites (ECC) composite beam with profiled steel sheeting. ce/papers, 2021, 4: 781-786. https://doi.org/10.1002/cepa.1361

[28] Nguyen C. L. and Lee C.K. Flexural behaviours of Engineered Cementitious Composites - High strength steel composite beams. Engineering Structures, 2021, 249. https://doi.org/10.1016/j.engstruct.2021.113324

[29] Lee S. W., Kang S.-B., Tan K. H., and Yang E.-H. Experimental and analytical investigation on bond-slip behaviour of deformed bars embedded in engineered cementitious composites. Construction and Building Materials, 2016, 127: 494-503. https://doi.org/10.1016/j.conbuildmat.2016.10.036

[30] Rana M. M., Lee C. K., and, Al-Deen S. A study on the bond stress-slip behavior between engineered cementitious composites and structural steel sections. Ce/papers, 2017, 1(2-3): 2247-2256. https://doi.org/10.1002/cepa.271

[31] Li V. C. On engineered cementitious composites (ECC) a review of the material and its applications. Journal of advanced concrete technology, 2003, 1(3): 215-230. https://doi.org/10.3151/jact.1.215

[32] Li V.C. Engineered Cementitious Composites (ECC): Bendable Concrete for Sustainable and Resilient Infrastructure, Springer, 2019. https://doi.org/10.1007/978-3-662-58438-5

[33] Emamjomeh H., Behfarnia K., Raji A., Almohammad-albakkar M. Influence of PVA and PP fibers addition on the durability and mechanical properties of engineered cementitious composites blended with silica fume and zeolite. Research on Engineering Structures and Materials, 2023; 9(2): 457-473. http://dx.doi.org/10.17515/resm2022.491me0804

[34] Yeşilmen S. Strength prediction of engineered cementitious composites with artificial neural networks. Research on Engineering Structures and Materials, 2021; 7(2): 173-182. https://doi.org/10.17515/resm2020.222ma1013

[35] Nguyen C.-L., and Lee C.-K. Development of analytical models for predicting the flexural behaviour of engineered cementitious composites-high strength steel composite beams. Advanced Steel Construction, 2023, 19(3): 197-208.

[36] Abaqus V. 6.14-1. Abaqus/standard user's manual and Abaqus CAE manual. Providence, RI, USA: Dassault Systemes Simulia Corp, 2014.

[37] Meng D., Huang T., Zhang Y. X., and Lee C. K. Mechanical behaviour of a polyvinyl alcohol fibre reinforced engineered cementitious composite (PVA-ECC) using local ingredients. Construction and Building Materials, 2017, 141: 259-270. https://doi.org/10.1016/j.conbuildmat.2017.02.158

[38] Katwal U., Tao Z., and Hassan M. K. Finite element modelling of steel-concrete composite beams with profiled steel sheeting. Journal of Constructional Steel Research, 2018, 146: 1-15. https://doi.org/10.1016/j.jcsr.2018.03.011

[39] Hassan M. K. Behaviour of hybrid stainless-carbon steel composite beam-column joints. Ph.D. Dissertation, Western Sydney University (Australia). 2016.